

Manifestation of incoherent-coherent crossover and non-Stoner magnetism in the electronic structure of Fe_3GeTe_2

Deepali Sharma,¹ Asif Ali,¹ Neeraj Bhatt,¹ Rajeswari Roy Chowdhury,¹
Chandan Patra,¹ Ravi Prakash Singh,¹ and Ravi Shankar Singh^{1, *}

¹*Department of Physics, Indian Institute of Science Education and Research Bhopal,
Bhopal Bypass Road, Bhauri, Bhopal 462066, India*

(Dated: August 29, 2024)

Two-dimensional (2D) van der Waals ferromagnets have potential applications as next-generation spintronic devices and provide a platform to explore the fundamental physics behind 2D magnetism. The dual nature (localized and itinerant) of electrons adds further complexity to the understanding of correlated magnetic materials. Here, we present the temperature evolution of electronic structure in 2D van der Waals ferromagnet, Fe_3GeTe_2 , using photoemission spectroscopy in conjunction with density functional theory (DFT) plus dynamical mean field theory (DMFT). With the appearance of quasiparticle peak and its evolution in the vicinity of Fermi energy, we unveil empirical evidences of incoherent-coherent crossover at around 125 K. DFT+DMFT results show that the quasiparticle lifetime surpasses thermal energy for temperature below 150 K, confirming incoherent-coherent crossover in the system. No appreciable change in the Fe $2p$ core level, overall valence band spectra across the magnetic transition, and temperature dependent ferromagnetic DFT+DMFT results, provide substantial evidence for non-stoner magnetism in Fe_3GeTe_2 . We elucidate the temperature dependent intimate relation between magnetism and electronic structure in Fe_3GeTe_2 . Sommerfeld coefficient of $\sim 104 \text{ mJ mol}^{-1} \text{ K}^{-2}$ obtained in the low temperature limit from DFT+DMFT calculations resolve the long standing issue of large Sommerfeld coefficient ($\sim 110 \text{ mJ mol}^{-1} \text{ K}^{-2}$) obtained from specific heat measurements.

I. INTRODUCTION

Magnetism in two-dimensional (2D) van der Waals (vdW) materials have been the subject of great interest for their ordered magnetic phases down to the monolayer limit [1–3]. The magnetic and electronic ground state of these 2D materials can be manipulated by external stimuli such as strain, gating, proximity effects, *etc.*, and the easy exfoliation allows the fabrication of novel devices down to the 2D limit [2, 3]. In this class of ferromagnets, $\text{Cr}_2\text{Ge}_2\text{Te}_6$, CrSiTe_3 , CrI_3 , *etc.* have been widely studied due to the rich interplay between long-range magnetic ordering, inter-site exchange (J), and intra-site coulomb (U) interactions in deciding the electronic structure [4–6].

Fe_3GeTe_2 , a 2D vdW ferromagnet, has gained enormous attention due to the remarkably high Curie temperature ($T_C \sim 220 \text{ K}$), large uniaxial magneto-crystalline anisotropy persisting down to the monolayer limit, magnetic skyrmions, anomalous Hall effect, *etc.* [7–10]. Density functional theory (DFT) reveals the itinerant ferromagnetism fulfilling the Stoner criteria [11, 12], which is supported by photoemission spectroscopy (PES) exhibiting continuous spectral weight transfer within Fe $3d$ states (signature of exchange splitting) in the ferromagnetic phase [13]. However, in complete contrast, another report using angle-resolved PES (ARPES) reveals insignificant change in the band dispersion with increasing temperature up to T_C [14].

In general, the nature of ferromagnetism is understood from [i] Stoner model in the case of itinerant bands where the temperature dependent exchange splitting of dispersive spin bands drive the long-range magnetic ordering, which eventually vanishes upon reaching T_C or [ii] spin mixing model in the case of localized bands where the exchange splitting exists even above T_C and the thermal fluctuation of the local moment reduces the magnetization [15–17]. However, many magnetic materials fall under the intermediate regime of itinerant-local moments, such as cuprates and iron-pnictides, due to a rich interplay of electronic states and magnetic correlations [15–21]. Despite being a d -electron system, coexisting localized as well as itinerant electrons drive Fe_3GeTe_2 to a heavy-fermionic state at low temperature [13, 22, 23]. The electronic transport and magnetic measurements indicate signature of incoherent-coherent crossover much below T_C , along with Fano-resonance feature in the scanning tunneling spectra concluding the Kondo scenario [13, 23, 24]. The large effective mass ($\sim 13.3 m_{\text{DFT}}$) from Sommerfeld coefficient ($\gamma = 110 \text{ mJ mol}^{-1} \text{ K}^{-2}$) obtained from specific heat measurements is not adequately reproduced from ARPES and dynamical mean field theory (DMFT) calculations across the literature [13, 14, 25, 26]. Understanding the nature of ferromagnetism (Stoner versus non-Stoner), incoherent-coherent crossover, and large effective mass leading to heavy-fermionic behavior warrants a comprehensive study of the electronic structure and its relation with magnetism in both high and low temperature limits.

Here, we investigate the electronic structure of Fe_3GeTe_2 using photoemission spectroscopy and theoretical calculations within DFT+DMFT framework. The

* rssingh@iiserb.ac.in

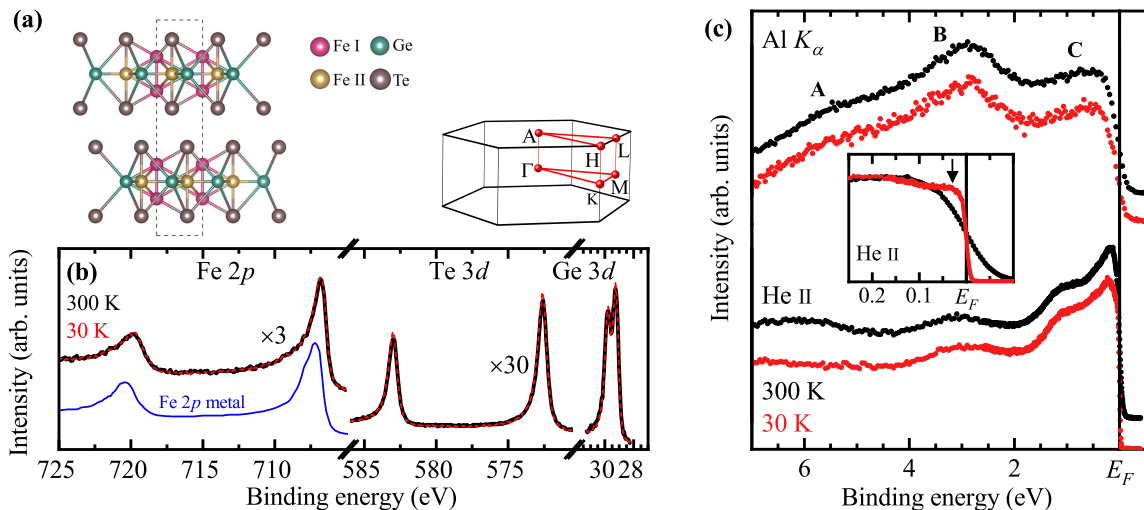


FIG. 1. (a) Crystal structure and Brillouin zone of Fe₃GeTe₂. The dashed line in the structure shows the unit cell comprising two formula units. (b) Core level photoemission spectra of Fe 2*p*, Te 3*d* and Ge 3*d* collected at 300 K (black) and 30 K (red) using Al *K* α (intensities are normalized to that of the survey scan, Fig. S1 of SM [27]). The spectra in blue line represent 2*p* core level of metal Fe in ferromagnetic regime, reproduced from [28]. (c) Valence band photoemission spectra collected using Al *K* α and He II radiations at 300 K (black) and 30 K (red). Inset shows He II spectra in the vicinity of E_F .

Fe 2*p* core level spectra as well as valence band spectra remain very similar across T_C , except for the states close to the Fermi level (E_F). High-resolution spectra unveils the emergence of a quasiparticle peak in the close vicinity of E_F in the magnetically ordered phase. The overall valence band spectra and evolution of quasiparticle peak, and manifestation of incoherent-coherent crossover (~ 125 K) in the experimental spectra, are very well captured within temperature dependent ferromagnetic DFT+DMFT calculations. These results further reveal spin-differentiated behavior in Fe₃GeTe₂, where spin-up states are majorly responsible for incoherent-coherent crossover with lowering temperature, whereas spin-down states are already in the coherent regime. Interestingly, finite spin splitting and the ordered moment persists even at temperature larger than $4T_C$, implies non-Stoner magnetism in Fe₃GeTe₂. Additionally, large Sommerfeld coefficient obtained in the low temperature limit from DFT+DMFT calculations are commensurate with results obtained from specific heat measurements resolving prior inconsistencies.

II. METHODOLOGY

High-quality single crystals of Fe₃GeTe₂ were prepared using chemical vapor transport method with I₂ as transport agent [9, 10]. Direction dependent magnetic measurements reveal the average Curie temperature, T_C to be 206 ± 4 K [9, 10]. Room temperature lattice parameters were found to be $a = b = 3.99$ Å and $c = 16.33$ Å in good agreement with previous report [29]. In the photoemission spectroscopic measurements, the Fermi level (E_F) positions and energy resolutions for various radi-

ations were obtained by measuring the Fermi-edge of a clean polycrystalline silver sample at 30 K. Total energy resolutions were set to 300 meV, 12 meV and 5 meV for Al *K* α ($h\nu = 1486.6$ eV), He II ($h\nu = 40.8$ eV) and He I ($h\nu = 21.2$ eV) radiations (energy), respectively. Multiple single crystals of Fe₃GeTe₂ were cleaved *in-situ* at base pressure better than 4×10^{-11} mbar, to ascertain the cleanliness of the sample surface and reproducibility of the data (see Supplemental Material (SM) [27] for survey scan and low energy electron diffraction (LEED)).

Electronic structure calculations were performed using experimental lattice parameters having two formula units (f.u.) per unit cell. Full-potential linearized augmented plane wave method as implemented in WIEN2K [30] was used for the DFT calculations. Generalized gradient approximation (GGA) of Perdew-Burke-Ernzerhof [31] was employed for the exchange correlation functional. $18 \times 18 \times 3$ *k*-mesh within the first Brillouin zone was used for the self-consistent calculations. The energy and charge convergence criteria were set to 10^{-4} eV and 10^{-4} electronic charge per f.u., respectively. eDMFT code [32] was used for the charge self-consistent DFT+DMFT calculations, with two impurity problems for Fe I and Fe II, and all five Fe 3*d* orbitals (forming three non-degenerate groups, d_{z^2} , $d_{x^2-y^2}/d_{xy}$ and d_{xz}/d_{yz}) were considered into correlated sub-space. The Continuous-Time Quantum Monte Carlo (CTQMC) impurity solver [33] was used with double counting correction as ‘exact’ [34]. The Hubbard- $U = 5.0$ eV and Hund’s coupling- $J = 0.9$ eV was opted for both Fe I and Fe II, in accordance with earlier report [26]. Analytical continuation was performed using maximum entropy method [32] to calculate self-energy on the real axis.

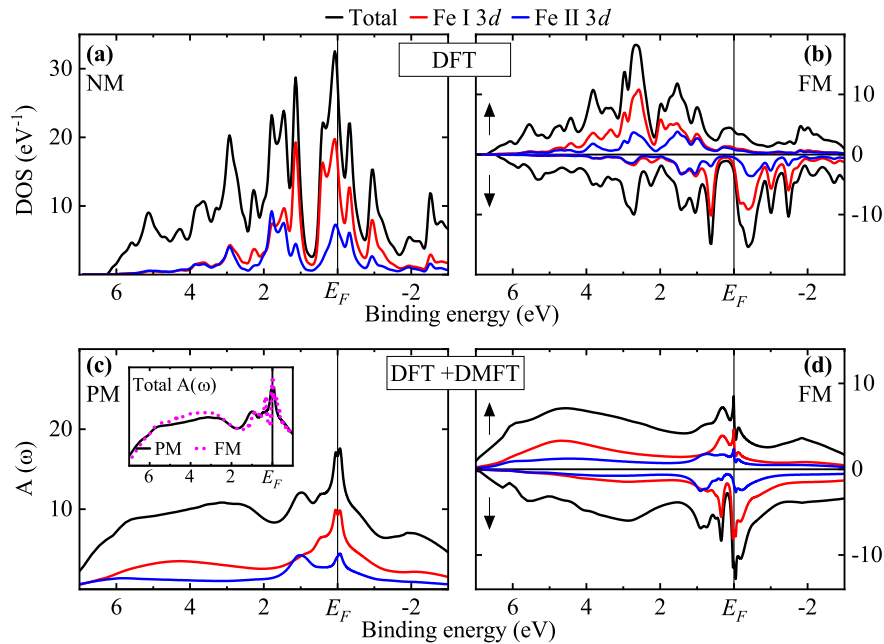


FIG. 2. Total DOS and partial DOSs of Fe I and Fe II for Fe_3GeTe_2 using (a) NM and (b) FM DFT. Total and partial spectral functions using DFT+DMFT in (c) PM ($T = 300$ K) and (d) FM ($T = 50$ K) phases. Inset in (c) shows the comparison of total spectral functions obtained in PM and FM DFT+DMFT phases.

III. RESULTS AND DISCUSSIONS

The crystal structure and Brillouin zone of Fe_3GeTe_2 are shown in Fig. 1 (a). Each vdW bonded layer comprises a Fe_3Ge slab sandwiched between Te layers. Two crystallographically different Fe sites are shown in pink (Fe I) and golden (Fe II) spheres [9, 11, 23]. High-quality of the sample and clean surface obtained by *in-situ* cleaving was ascertained by the sharpness of peaks and the absence of any oxide-related features in the core level spectra, as shown in Fig. 1 (b) (also see Note 1 of SM [27] for further details). All the core level spectra remain very similar to their elemental counterparts [35]. No appreciable change was observed for all the core levels while going from 300 K to 30 K. Notably, the width of Fe $2p$ core level spectra in Fe_3GeTe_2 is comparable to that of ferromagnet iron (shown by blue lines) while it has been found to be much smaller (~ 0.6 eV) in the non-magnetic systems [28, 36]. The full width at half maxima (FWHM) of the asymmetric Fe $2p_{3/2}$ peak was estimated (after subtracting a Shirley type integral background), where the FWHM was obtained to be ~ 1.2 eV and ~ 1.4 eV for Fe_3GeTe_2 and Fe metal, respectively. The larger width arises due to finite exchange splitting leading to observed dichroism in the core level spectra in the case of magnetic systems [28, 37, 38]. No change in Fe $2p$ core level spectra in Fe_3GeTe_2 suggests that the exchange splitting does not change appreciably across T_C , indicating that the non-Stoner behavior may be applicable here. The valence band in Fe_3GeTe_2 is formed by the hybridization of mainly Fe $3d$, Ge $4p$ and Te $5p$ states,

and has been shown in Fig. 1 (c) collected using Al K_α and He II radiations across the magnetic phase transition. Al K_α spectra at 300 K exhibit three discernible features A, B, and C at around 6 eV, 3 eV and a broad feature below 2 eV binding energy (BE), respectively. Relative intensity enhancement of feature C with respect to features A and B while going from Al K_α spectra to He II spectra can be understood considering the larger photoionization cross-section of Fe $3d$ states to that of Te $5p$ and Ge $4p$ states at lower photon energies [39], confirming the dominant contribution of Fe $3d$ states in feature C. Also, the broad feature C in Al K_α spectra is further resolved in the He II spectra, presumably due to better energy resolution, exhibiting a peak near E_F and a shoulder structure at 1 eV BE. Surprisingly, the overall valence band spectra also do not show appreciable change across the magnetic phase transition which is in sharp contrast with the prototypical itinerant ferromagnet SrRuO_3 [40, 41], except for the states in the close vicinity of E_F , as shown in the inset of Fig. 1 (c) where the signature of a quasiparticle peak (marked by down arrow) at 30 K is evident (will be further discussed in the high-resolution spectra).

To understand the subtle changes in the electronic structure across the magnetic phase transition, we discuss the results of the DFT calculations. Similar to experimental observations, calculated density of states (DOSs) in non-magnetic (NM) phase reveal predominant Fe $3d$ states between ± 2 eV BE (shown in Fig. 2 (a)), with large states at E_F indicating metallic character. The states corresponding to Ge $4p$ and Te $5p$ pri-

marily appear at higher BE (Fig. S3 [27] of SM). As expected, the total energy per unit cell reduces by 130 meV in the ferromagnetic (FM) phase and the resulting spin-polarized DOSs are shown in Fig. 2 (b). Large redistribution of exchange split spin-polarized states in FM phase compared to NM phase, substantial Fe 3d states appearing even beyond 2 eV BE, along with much reduced $\text{DOS}(E_F)$, are in sharp contrast with the experimental observations. The obtained average magnetic moment of about $2.2 \mu_B/\text{Fe}$ is also an overestimation from the value ($1.6 \mu_B/\text{Fe}$) obtained from the magnetic measurements [9]. Even the inclusion of Hubbard- U in DFT+ U does not reproduce the experimental results (see Fig. S4 and S5 of SM [27]). These observations are consistent with earlier studies, concluding that the DFT and DFT+ U fails to achieve an agreement with the experimental lattice parameters, magnetic moment and valence band spectra in the magnetically ordered phase [25, 42].

Having an admixture of localized and itinerant d electrons, Fe_3GeTe_2 has been understood as correlated electron system with significant role of Hund's- J [43]. DFT+DMFT has been quite successful in accurately describing such systems with various magnetic transitions [44, 45], since it captures the fluctuating moment in the paramagnetic (PM) phase, along with temperature dependent moment in the magnetically ordered phase [45–47]. In Fig. 2 (c), we show the PM DFT+DMFT results for $T = 300$ K ($\beta = 38.68 \text{ eV}^{-1}$), where renormalized Fe 3d bands appear between ± 1.5 eV BE. The total spectral function exhibiting a peak around E_F along with a hump at 1 eV BE are in excellent agreement with the He II spectra at 300 K. The local spin moment was found to be $1.72 \mu_B/\text{Fe}$ in PM DFT+DMFT, calculated using $\sum_i 2P_i|S_i^z|$ (where P_i and $|S_i^z|$ represent the probability and absolute spin moment, respectively). The FM DFT+DMFT result for $T = 50$ K ($\beta = 232 \text{ eV}^{-1}$) shown in Fig. 2 (d) exhibits quasiparticle peak at E_F in the exchange split spin-polarized spectral functions corresponding to both the Fe sites. The total spectral function remains largely unchanged while going from PM to FM phase, as shown in the inset of Fig. 2 (c). Further, the magnetic moment of $1.51 \mu_B/\text{Fe}$ in the FM phase is in close agreement with the experimental saturation moment [9] and closely approaches local spin moment obtained in the PM phase. Thus, DFT+DMFT framework successfully determines the electronic structure of Fe_3GeTe_2 in both the PM and FM phases.

For further understanding of the evolution of electronic states with temperature, we show the temperature dependent high-resolution valence band spectra collected using He I radiation in the top panel of Fig. 3 (a). All the spectra are normalized by the total integrated intensity below 1.5 eV BE and have been stacked vertically for clarity. The 250 K spectra exhibit a hump-like structure at ~ 1 eV BE and a broader feature below 0.5 eV BE, similar to high temperature He II spectra (Fig. 1 (c)). With lowering temperature, the spectral weight redistribu-

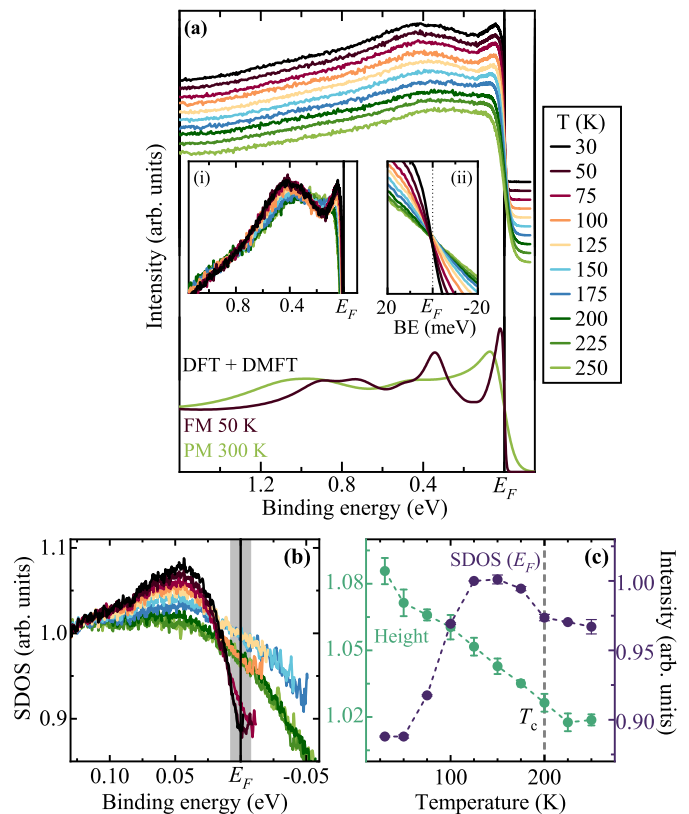


FIG. 3. (a) Temperature dependent high-resolution valence band spectra collected using He I. Lower panel shows the occupied part of DFT+DMFT spectral function for PM (300 K) and FM (50 K) phases. Inset (i): T -dependent spectral weight redistribution. Inset (ii): T evolution of the spectra in the close vicinity of E_F . T -dependent (b) SDOS in the vicinity of E_F , (c) quasiparticle peak height (green) and $\text{SDOS}(E_F)$ (purple) obtained from (b). Shaded region in (b) represents $\pm 3k_B T$ range at 30 K.

tion is evident leading to the appearance of sharper quasiparticle peak below 50 meV as shown in the inset (i), while broad feature at 0.4 eV BE remains very similar (within ± 0.05 eV). It is to be noted here that the energy distribution curves (EDC) at various k -points from low temperature ARPES is very similar to the angle-integrated spectra shown here (see APPENDIX I). The lower panel shows the DFT+DMFT spectral function ($A(\omega)$) obtained in PM ($T = 300$ K) and FM ($T = 50$ K) phases multiplied by the Fermi-Dirac (FD) function to mimic the occupied states across T_C exhibiting remarkable resemblance of the spectral evolution with the experimental spectra with respect to overall width and energy positions of the features. To visualize the change in the electronic states in the close vicinity of E_F , we normalize the spectral intensity at 150 meV and a closer look reveals that the temperature evolution is similar to FD function with a small decrease of the intensity at E_F for low temperature spectra, as shown in the inset (ii). We further show the spectral DOS (SDOS) in Fig. 3 (b) obtained by dividing the photoemission intensity

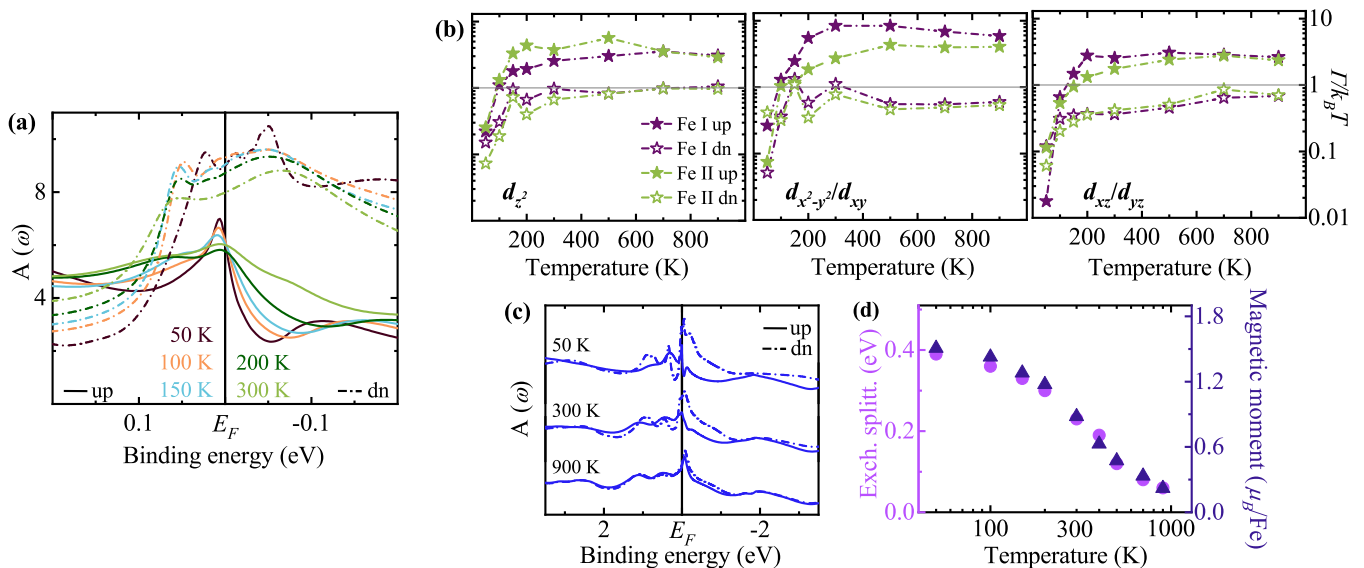


FIG. 4. Temperature dependent FM DFT+DMFT results. (a) Spin-up (solid line) and spin-down (dash-dot line) Fe 3d spectral functions. (b) $\Gamma/k_B T$ for the three non-degenerate orbitals (including both the spin) for both the Fe. Spin-up (closed markers) and spin-down (open markers) for Fe I (dark pink) and Fe II (green). (c) Spin-polarized total spectral functions, (d) exchange splitting (circles) and magnetic moments (triangles) at various temperature.

with the resolution broadened FD function at respective temperatures [48]. The evident emergence of quasiparticle peak at ~ 40 meV BE upon entering the FM phase is shown by the monotonous increase in its height and plotted in Fig. 3 (c) (using green symbols). Interestingly, SDOS(E_F) exhibit complex/unusual evolution with temperature, as shown in Fig. 3 (c) (using purple symbols). SDOS(E_F) remains very similar in the PM phase, while it increases upon entering the magnetic phase and achieves a maxima at ~ 125 K, below which it decreases down to 50 K and saturates at lower temperature (also observed in SDOS obtained by symmetrizing the spectra [49], Fig. S2 of SM [27]). A change of slope in the resistivity of Fe₃GeTe₂ near a characteristic temperature ($T^* \sim 110$ K) [13, 23] has been associated with an incoherent to coherent crossover similar to the f -electron based heavy fermionic systems [50–52]. Below T^* , the concept of quasiparticle becomes meaningful as the quasiparticle scattering rate, Γ (inverse of the lifetime), is smaller than the thermal energy ($k_B T$) and sharper quasiparticle features can be observed [53]. The SDOS obtained from the high-resolution spectra (shown in Fig. 3 (b)) reveals decrease in the width of quasiparticle peak below 125 K, also manifested by the sharp decrease of SDOS(E_F) as shown in Fig. 3 (c).

We additionally showcase and meticulously explore these phenomenon using temperature dependent FM DFT+DMFT calculations. The evolution of the quasiparticle peak with decreasing temperature is also well captured within the FM DFT+DMFT calculations, where the spin-polarized Fe spectral functions are shown in Fig. 4 (a). Intriguingly, we observe that the spin-down spectral functions remain largely unchanged around the

E_F , however, the spin-up spectral functions demonstrate the emergence of quasiparticle peak just below E_F with decreasing temperature, implying significant influence of spin-differentiated electron correlation in Fe₃GeTe₂. Further, the scattering rate, Γ was obtained for all the orbitals (including spin) for both the Fe sites (see APPENDIX II) and $\Gamma/k_B T$ for various temperature is shown in Fig. 4 (b). These results unveiled that the Γ for spin-down channels for both the Fe sites remain below $k_B T$, irrespective of temperature, suggesting the coherent scenario, while the spin-up channels show an incoherent-coherent crossover only below 150 K. It is to be noted that, the zero frequency limit of the imaginary part of the self-energy on the imaginary frequency axis, $\text{Im}\Sigma(i\omega \rightarrow 0^+)$, and thus the Γ approach to zero faster with decreasing temperature for the spin-up channels than those for the spin-down channels for all the orbitals of both the Fe sites.

Within the itinerant electron magnetism, the exchange splitting of non-degenerate spin bands can be defined via various approaches [11, 14, 40, 42, 54]. In the DFT band scenario, the k -dependent exchange splitting can be estimated from the difference of the Kohn-Sham eigenvalues of spin split bands and the k -averaging gives a reasonable estimate [11]. However, the similar analysis can not be performed in DFT+DMFT due to the diffusive/incoherent nature of the k -resolved spectral function [42]. Here, we attempt to estimate the exchange splitting in the Fe bands from the energy difference of the centre of the weight of spin-up and spin-down from k -integrated spectral functions. The calculated spin-polarized total spectral functions are shown in Fig. 4 (c) for different temperatures. The spectral function at 50 K reveal

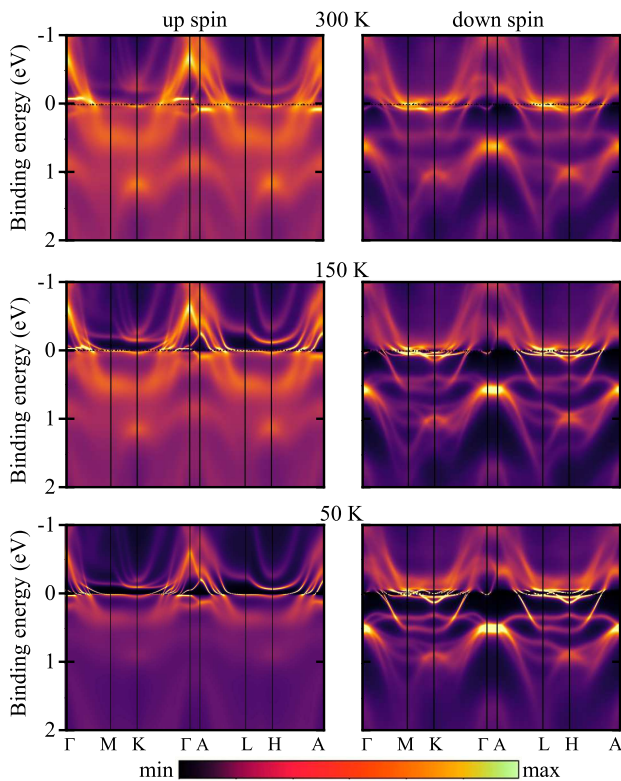


FIG. 5. k -resolved spectral functions from FM DFT+DMFT for the spin-up (left) and spin-down (right) at 300 K, 150 K and 50 K.

large exchange splitting, which reduces with increasing temperature where, both spin-up and spin-down spectral functions try to acquire similar structure. Interestingly, the spin-dependent spectral functions remain non-degenerate even above T_C and further upto 900 K. The estimated exchange splitting and obtained magnetic moment also follows the similar trend, and remains finite upto 900 K, as shown in Fig. 4 (d).

To further elucidate the spin-differentiated dual nature, k -resolved spin-polarized spectral functions for different temperature obtained from FM DFT+DMFT calculations are shown in Fig. 5. Large number of dispersive bands in both the spin channels show finite exchange splitting and confirm the itinerant character, while the non-dispersive bands in the vicinity of E_F in case of spin-down channel, at high-temperature suggests mixture of localized and itinerant electrons in Fe_3GeTe_2 . Electronic structure calculations within DFT+DMFT framework hugely overestimates the ferromagnetic transition and reveals no significant change in the valence band across T_C , hence, providing additional evidence to conclude Fe_3GeTe_2 to be non-Stoner where, the temporal and spatial thermal fluctuation leads to disordered moment (itinerant and local both) thereby destroying the long range magnetic order beyond T_C . The Stoner model provides framework for the itinerant magnetic materials, however the inaccurate consideration of spin density fluctuation

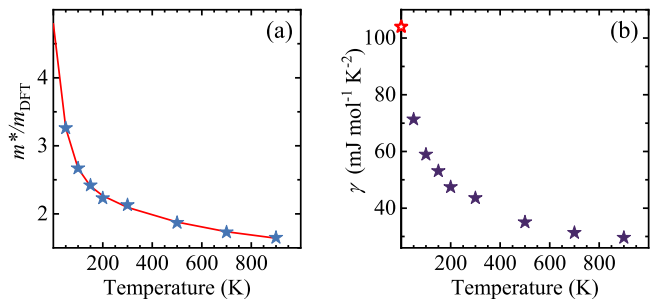


FIG. 6. Calculated (a) mass enhancement factor (m^*/m_{DFT}) and (b) Sommerfeld coefficient (γ) using FM DFT+DMFT calculations at various temperature. The red line in (a) shows the fitting using double exponential function ($y_0 + a_1e^{(-x/t_1)} + a_2e^{(-x/t_2)}$), where $y_0=1.45$, $a_1=2.17$, $a_2=1.17$, $t_1=47.03$ and $t_2=498.22$) and the open star in (b) shows calculated γ obtained using extrapolated value of mass enhancement factor at 0 K.

effects results in many limitations like overestimating T_C and Curie-Weiss behavior at higher temperature [15, 29]. Thus, these results encourage the need for spin-resolved (AR)PES to be examined for further understanding of the electronic structure of Fe_3GeTe_2 across T_C . In addition, diffusive bands in spin-up k -resolved spectral functions representing incoherent states show crossover to sharp/coherent states with lowering temperature while spin-down channels remain very similar. The spectral function obtained from low temperature DFT+DMFT are in reasonable agreement with experimental band dispersion along M- Γ -K directions (shown in APPENDIX I). Further, observed dispersive energy bands along Γ -A direction in k -resolved spectral functions at low temperature implies significant interlayer coupling, thus three-dimensionality of electronic structure in Fe_3GeTe_2 [14]. Lower Fermi velocity of spin split bands in Fe_3GeTe_2 than that in the case of a typical metal along with hybridisation of these flat bands with strongly dispersive bands near E_F , suggest strengthened quasiparticle mass [13, 24].

Finally, we discuss the discrepancy related to mass enhancement factor (m^*/m_e) in the literature [13, 14, 25, 26, 43]. The Sommerfeld coefficient, γ ($110 \text{ mJ mol}^{-1} \text{ K}^{-2}$) obtained from specific heat measurement is much larger than that of the free electron value of $\approx 6 \text{ mJ mol}^{-1} \text{ K}^{-2}$ considering six electron occupancy per Fe, leading to the heavy-fermionic system with m^*/m_e of ≈ 18 [25, 55]. As discussed earlier, the large reduction of $\text{DOS}(E_F)$ obtained in FM DFT results (*w.r.t.* NM DFT results) is in strong disagreement with PES results and also leads to an overestimation of the $\frac{m^*}{m_{\text{DFT}}} = 14.12$ (see Fig. S4 of SM [27]). Within DFT+DMFT framework, $\frac{m^*}{m_{\text{DFT}}}$ is weighted sum of contributions arising from all the orbital (l) and spin (s), weighted by their local Green's function (\propto partial DOS) at E_F [43, 45]. The $\frac{m^*}{m_{\text{DFT}}}$ obtained from FM DFT+DMFT calculations as shown in Fig. 6 (a), unveils increasing mass enhancement with lowering

temperature and having $\frac{m^*}{m_{\text{DFT}}} = 3.26$ at 50 K, suggesting Fe_3GeTe_2 to be heavy fermionic system at low temperature. The γ_{DMFT} obtained by linear sum of each contribution, $\gamma_{l,s}$, ($\gamma_{\text{DMFT}} = \sum_{l,s} \gamma_{l,s} = \sum_{l,s} [(\pi^2 k_B^2/3) \frac{m^*}{m_b} \rho_{l,s}^{\text{PDOS}}] \approx [(\pi^2 k_B^2/3) \frac{m^*}{m_{\text{DFT}}} A(\omega)]$ [45] lead to ~ 70 mJ mol $^{-1}$ K $^{-2}$ at 50 K. The extrapolated value of $\frac{m^*}{m_{\text{DFT}}}$ of 4.79 at 0 K leads to γ of about ~ 104 mJ mol $^{-1}$ K $^{-2}$, as shown in Fig. 6 (b) and is in close agreement with experiments, finally resolving the much debated disparity [25].

IV. CONCLUSION

In summary, electronic structure of Fe_3GeTe_2 has been investigated using photoemission spectroscopy and theoretical calculations within DFT, DFT+ U and DFT+DMFT frameworks. The high-resolution valence band spectra are well captured within DFT+DMFT across the magnetic phase transition. Temperature dependent high-resolution spectra exhibit emergence of quasiparticle peak in close vicinity of E_F along with the manifestation of incoherent-coherent crossover where, an anomalous behaviour of spectral density of states at E_F is observed ~ 125 K. DFT+DMFT successfully demonstrate the evolution of spin bands with incoherent-coherent crossover along with the increasing effective mass at lower temperatures, concluding the heavy-fermionic nature. We also resolves the long standing issue of large Sommerfeld coefficient in this system obtained within DFT+DMFT calculations. In particular, (i) no significant change in the experimental Fe 2*p* core level and overall valence band across T_C , and (ii) finite exchange splitting (also magnetic moment) persisting even beyond $4T_C$ in temperature dependent ferromagnetic DFT+DMFT calculations, together suggests Fe_3GeTe_2 to be a non-Stoner ferromagnet. Results presented here advances the understanding of complex evolution of electronic structure and non-Stoner magnetic behavior and lays the foundation for further spin-resolved PES in this correlated van der Waals ferromagnet Fe_3GeTe_2 .

ACKNOWLEDGMENTS

D. S. and N. B. acknowledge the Council of Scientific and Industrial Research (CSIR), Government of India, for financial support with Award No. 09/1020(0198)/2020-EMR-I and 09/1020(0177)/2019-EMR-I, respectively. R.R.C. acknowledges the Department of Science and Technology (DST), Government of India, for financial support (Grant No. DST/INSPIRE/04/2018/001755). R.P.S. acknowledges the Science and Engineering Research Board (SERB), Government of India, for Core Research Grant No. CRG/2019/001028. We gratefully acknowledge the use of HPC facility and CIF at IISER Bhopal.

APPENDIX I

ARPES Fermi surface map (integrated within $E_F \pm 10$ meV energy window and symmetrized along $k_x = 0$ line) obtained using He I radiation ($k_z = 0.353c^*$, considering inner potential, $V_0=13.5$ eV [14]) at 30 K (with total energy resolution ~ 15 meV) is shown in Fig. 7 (a). The circular and hexagonal shaped Fermi surfaces centered around $\bar{\Gamma}$ is in agreement with earlier observations [13, 14]. Fig. 7(b) shows the schematic of the obtained Fermi surfaces where the dotted red hexagon represents the surface Brillouin zone with high symmetry lines $\bar{\Gamma}-\bar{K}$, and $\bar{\Gamma}-\bar{M}$. The stars represents $\bar{\Gamma}$, $(\bar{\Gamma}-\bar{M})/2$ and $(\bar{\Gamma}-\bar{K})/2$, corresponding to which the energy distributive curves (EDCs) (integrated for Δk_x and Δk_y within $\pm 0.02 \text{ \AA}^{-1}$) are shown in Fig. 7 (c). Strengthened quasiparticle peak (~ 40 meV BE) is evident from the EDC at $\bar{\Gamma}$, as compared to the same obtained from EDC at $(\bar{\Gamma}-\bar{M})/2$ and $(\bar{\Gamma}-\bar{K})/2$. It is to be noted that the overall EDCs at various locations across Brillouin zone are mostly similar and agrees well with the momentum-integration high-resolution PES spectra as presented in the main text (Fig. 3 (a)). Further, Fig. 7 (d) and (e) represent the band dispersion from ARPES (at 30 K) and k -resolved spectral functions of both the spins from FM DFT+DMFT calculation (at 50 K, $k_z = 0.353c^*$), respectively, along high-symmetry directions. ARPES spectra (Fig. 7 (d)) shows broad (incoherent like) bands at around 0.4 eV BE and sharper (coherent like) bands around the E_F in $\bar{M}-\bar{\Gamma}$ as well as in $\bar{\Gamma}-\bar{K}$ directions, which are better resolved in both the spin channels of k -resolved spectral functions of DFT+DMFT. For better visualization, the bands with higher spectral functions from DFT+DMFT results were overlapped on the ARPES spectra (using markers) and is shown in Fig. 7 (d) with up and down green triangles for up spin and for down spin, respectively.

APPENDIX II

Within FM DFT+DMFT calculation the spin and orbital dependent imaginary part of the self-energy on the Matsubara frequency axis, $\text{Im}\Sigma(i\omega)$ for both Fe sites were obtained and are shown in Fig. 8 (a) for $T = 50$ K. The $\text{Im}\Sigma(i\omega)$ approaches to zero at lower frequency for all the orbitals and spins of both the Fe. The quasiparticle scattering rate is calculated using $\Gamma_{l,s} = -(m^*/m_b)_{l,s}^{-1} \text{Im}\Sigma_{l,s}(i\omega \rightarrow 0^+)$, where $(m^*/m_b)_{l,s} = 1 - \partial \text{Im}\Sigma_{l,s}(i\omega)/\partial(i\omega)|_{i\omega \rightarrow 0}$ for l orbitals, and s spins, and is shown in Fig. 8 (b) [43, 45] for various temperatures. The imaginary part of self energy at the zero frequency limit and its derivative was obtained using fourth order polynomial fit for the first six data points. The spin-up channels for both the Fe exhibit larger $\text{Im}\Sigma_l(i\omega \rightarrow 0^+)$ for all the orbitals at higher temperature and tends to zero faster at lower temperature in comparison to that for the spin down channels, implying significant influence of

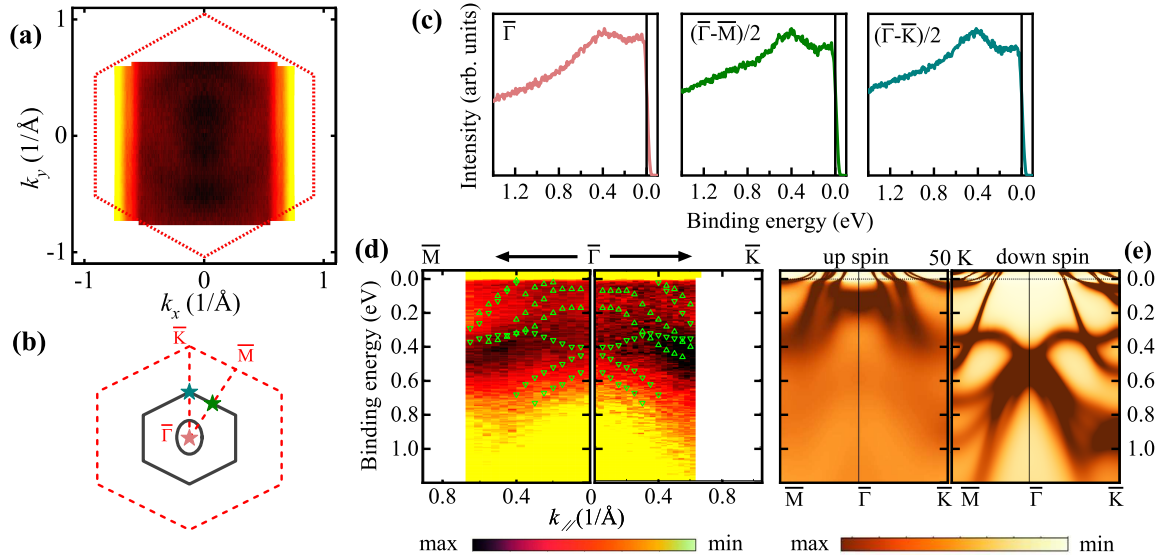


FIG. 7. Fermi surface map of Fe_3GeTe_2 (a) using He I radiation at 30 K, and (b) schematic diagram. The red dashed line shows the Brillouin zone with high-symmetry directions in (b). The stars marked in (b) with pink, green and blue colour represents $\bar{\Gamma}$, $(\bar{\Gamma}-\bar{M})/2$ and $(\bar{\Gamma}-\bar{K})/2$ locations, respectively, along which (c) energy distribution curves are shown. (d) ARPES band dispersion and (e) k -resolved spectral function at $k_z = 0.353c^*$ from FM DFT+DMFT ($T = 50$ K) for both the spin bands, along the high-symmetry directions. For better visualization the high intensity bands from up and down spin of k -resolved spectral functions, were overlapped on ARPES band dispersion using up and down green triangles, respectively.

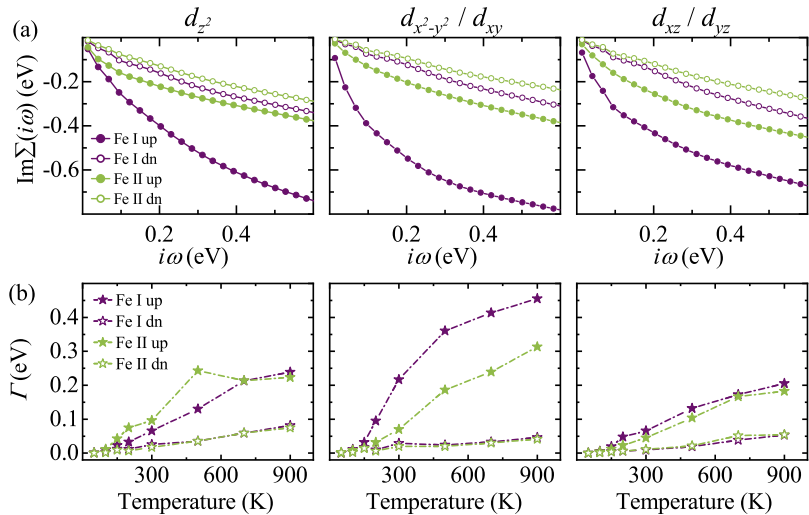


FIG. 8. (a) Spin and orbital dependent imaginary part of self-energy on Matsubara frequency axis, $\text{Im}\Sigma(i\omega)$ for both the Fe using FM DFT+DMFT calculations at 50 K. (b) Quasiparticle scattering rate (Γ) for the three non-degenerate orbitals (including spin) for both the Fe at various temperatures. Spin-up and spin-down are shown in closed markers and open markers, respectively for Fe I (dark pink) and Fe II (green).

spin-differentiated electron correlation in Fe_3GeTe_2 . An overall trend of $\Gamma_{l,s}$ is consistent with the imaginary part of self energy at the zero frequency limit. Further, the Γ obtained for all the orbitals for both the Fe sites, unveiled that the spin-down channels remain below $k_B T$ (as

shown in Fig. 4 (b)), irrespective of temperature for both the Fe sites, suggesting the coherent scenario throughout, while the spin-up channels show an incoherent-coherent crossover only below 150 K.

-
- [1] K. F. Mak, J. Shan, and D. C. Ralph, Probing and controlling magnetic states in 2D layered magnetic materials, *Nature Reviews Physics* **1**, 646 (2019).
- [2] M. Gibertini, M. Koperski, A. F. Morpurgo, and K. S. Novoselov, Magnetic 2D materials and heterostructures, *Nature Nanotechnology* **14**, 408 (2019).
- [3] K. S. Burch, D. Mandrus, and J.-G. Park, Magnetism in two-dimensional van der Waals materials, *Nature* **563**, 47 (2018).
- [4] C. Gong, L. Li, Z. Li, H. Ji, A. Stern, Y. Xia, T. Cao, W. Bao, C. Wang, Y. Wang, Z. Q. Qiu, R. J. Cava, S. G. Louie, J. Xia, and X. Zhang, Discovery of intrinsic ferromagnetism in two-dimensional van der Waals crystals, *Nature* **546**, 265 (2017).
- [5] T. J. Williams, A. A. Aczel, M. D. Lumsden, S. E. Nagler, M. B. Stone, J.-Q. Yan, and D. Mandrus, Magnetic correlations in the quasi-two-dimensional semiconducting ferromagnet CrSiTe_3 , *Phys. Rev. B* **92**, 144404 (2015).
- [6] B. Huang, G. Clark, E. Navarro-Moratalla, D. R. Klein, R. Cheng, K. L. Seyler, D. Zhong, E. Schmidgall, M. A. McGuire, D. H. Cobden, W. Yao, D. Xiao, P. Jarillo-Herrero, and X. Xu, Layer-dependent ferromagnetism in a van der Waals crystal down to the monolayer limit, *Nature* **546**, 270 (2017).
- [7] Y. Deng, Y. Yu, Y. Song, J. Zhang, N. Z. Wang, Z. Sun, Y. Yi, Y. Z. Wu, S. Wu, J. Zhu, J. Wang, X. H. Chen, and Y. Zhang, Gate-tunable room-temperature ferromagnetism in two-dimensional Fe_3GeTe_2 , *Nature* **563**, 94 (2018).
- [8] M. T. Birch, L. Powalla, S. Wintz, O. Hovorka, K. Litzius, J. C. Loudon, L. A. Turnbull, V. Nehruji, K. Son, C. Bubeck, T. G. Rauch, M. Weigand, E. Goering, M. Burghard, and G. Schütz, History-dependent domain and skyrmion formation in 2D van der Waals magnet Fe_3GeTe_2 , *Nature Communications* **13**, 3035 (2022).
- [9] R. R. Chowdhury, S. DuttaGupta, C. Patra, O. A. Tretiakov, S. Sharma, S. Fukami, H. Ohno, and R. P. Singh, Unconventional Hall effect and its variation with Co-doping in van der Waals Fe_3GeTe_2 , *Scientific Reports* **11**, 14121 (2021).
- [10] R. Roy Chowdhury, C. Patra, S. DuttaGupta, S. Satheesh, S. Dan, S. Fukami, and R. P. Singh, Modification of unconventional Hall effect with doping at the nonmagnetic site in a two-dimensional van der Waals ferromagnet, *Phys. Rev. Materials* **6**, 014002 (2022).
- [11] H. L. Zhuang, P. R. C. Kent, and R. G. Hennig, Strong anisotropy and magnetostriction in the two-dimensional Stoner ferromagnet Fe_3GeTe_2 , *Phys. Rev. B* **93**, 134407 (2016).
- [12] D. Yuan, S. Jin, N. Liu, S. Shen, Z. Lin, K. Li, and X. Chen, Tuning magnetic properties in quasi-two-dimensional ferromagnetic $\text{Fe}_{3-y}\text{Ge}_{1-x}\text{As}_x\text{Te}_2$ ($0 \leq x \leq 0.85$), *Materials Research Express* **4**, 036103 (2017).
- [13] Y. Zhang, H. Lu, X. Zhu, S. Tan, W. Feng, Q. Liu, W. Zhang, Q. Chen, Y. Liu, X. Luo, D. Xie, L. Luo, Z. Zhang, and X. Lai, Emergence of Kondo lattice behavior in a van der Waals itinerant ferromagnet, Fe_3GeTe_2 , *Science Advances* **4**, eaao6791 (2018).
- [14] X. Xu, Y. W. Li, S. R. Duan, S. L. Zhang, Y. J. Chen, L. Kang, A. J. Liang, C. Chen, W. Xia, Y. Xu, P. Malinowski, X. D. Xu, J.-H. Chu, G. Li, Y. F. Guo, Z. K. Liu, L. X. Yang, and Y. L. Chen, Signature for non-Stoner ferromagnetism in the van der Waals ferromagnet Fe_3GeTe_2 , *Phys. Rev. B* **101**, 201104 (2020).
- [15] J. M. Santiago, C.-L. Huang, and E. Morosan, Itinerant magnetic metals, *J. Phys.: Condens. Matter* **29**, 373002 (2017).
- [16] V. Korenman, J. L. Murray, and R. E. Prange, Local-band theory of itinerant ferromagnetism. I. Fermi-liquid theory, *Phys. Rev. B* **16**, 4032 (1977).
- [17] K. Maiti, M. C. Malagoli, A. Dallmeyer, and C. Carbone, Finite Temperature Magnetism in Gd: Evidence against a Stoner Behavior, *Phys. Rev. Lett.* **88**, 167205 (2002).
- [18] D. C. Johnston, The puzzle of high temperature superconductivity in layered iron pnictides and chalcogenides, *Advances in Physics* **59**, 803 (2010).
- [19] P. Hansmann, R. Arita, A. Toschi, S. Sakai, G. Sangiovanni, and K. Held, Dichotomy between large local and small ordered magnetic moments in iron-based superconductors, *Phys. Rev. Lett.* **104**, 197002 (2010).
- [20] P. Dai, J. Hu, and E. Dagotto, Magnetism and its microscopic origin in iron-based high-temperature superconductors, *Nature Physics* **8**, 709 (2012).
- [21] K. Haule and G. Kotliar, Coherence-incoherence crossover in the normal state of iron oxypnictides and importance of Hund's rule coupling, *New Journal of Physics* **11**, 025021 (2009).
- [22] X. Bai, F. Lechermann, Y. Liu, Y. Cheng, A. I. Kolesnikov, F. Ye, T. J. Williams, S. Chi, T. Hong, G. E. Granroth, A. F. May, and S. Calder, Antiferromagnetic fluctuations and orbital-selective mott transition in the van der waals ferromagnet Fe_3GeTe_2 , *Phys. Rev. B* **106**, L180409 (2022).
- [23] M. Zhao, B.-B. Chen, Y. Xi, Y. Zhao, H. Xu, H. Zhang, N. Cheng, H. Feng, J. Zhuang, F. Pan, X. Xu, W. Hao, W. Li, S. Zhou, S. X. Dou, and Y. Du, Kondo Holes in the Two-Dimensional Itinerant Ising Ferromagnet Fe_3GeTe_2 , *Nano Letters* **21**, 6117 (2021).
- [24] D. Rana, A. R. B. G. C. Patra, S. Howlader, R. R. Chowdhury, M. Kabir, R. P. Singh, and G. Sheet, Spin-polarized supercurrent through the van der Waals Kondo-lattice ferromagnet Fe_3GeTe_2 , *Phys. Rev. B* **106**, 085120 (2022).
- [25] J.-X. Zhu, M. Janoschek, D. S. Chaves, J. C. Cezar, T. Durakiewicz, F. Ronning, Y. Sassa, M. Mansson, B. L. Scott, N. Wakeham, E. D. Bauer, and J. D. Thompson, Electronic correlation and magnetism in the ferromag-

- netic metal Fe_3GeTe_2 , *Phys. Rev. B* **93**, 144404 (2016).
- [26] K. Kim, J. Seo, E. Lee, K.-T. Ko, B. S. Kim, B. G. Jang, J. M. Ok, J. Lee, Y. J. Jo, W. Kang, J. H. Shim, C. Kim, H. W. Yeom, B. Il Min, B.-J. Yang, and J. S. Kim, Large anomalous Hall current induced by topological nodal lines in a ferromagnetic van der Waals semimetal, *Nature Materials* **17**, 794 (2018).
- [27] See Supplemental Material at [URL will be inserted by publisher] for experimental details and analysis and for further DFT and DFT+DMFT results..
- [28] G. Rossi, G. Panaccione, F. Sirotti, S. Lizzit, A. Baraldi, and G. Paolucci, Magnetic dichroism in the angular distribution of Fe $2p$ and $3p$ photoelectrons: Empirical support to zeeman-like analysis, *Phys. Rev. B* **55**, 11488 (1997).
- [29] B. Chen, J. Yang, H. Wang, M. Imai, H. Ohta, C. Michioka, K. Yoshimura, and M. Fang, Magnetic Properties of Layered Itinerant Electron Ferromagnet Fe_3GeTe_2 , *J. Phys. Soc. Jpn.* **82**, 124711 (2013).
- [30] P. Blaha, K. Schwarz, F. Tran, R. Laskowski, G. K. H. Madsen, and L. D. Marks, Wien2k: An APW+lo program for calculating the properties of solids, *J. Chem. Phys.* **152**, 074101 (2020).
- [31] J. P. Perdew, K. Burke, and M. Ernzerhof, Generalized Gradient Approximation Made Simple, *Phys. Rev. Lett.* **77**, 3865 (1996).
- [32] K. Haule, C.-H. Yee, and K. Kim, Dynamical mean-field theory within the full-potential methods: Electronic structure of CeIrIn_5 , CeCoIn_5 , and CeRhIn_5 , *Phys. Rev. B* **81**, 195107 (2010).
- [33] K. Haule, Quantum Monte Carlo impurity solver for cluster dynamical mean-field theory and electronic structure calculations with adjustable cluster base, *Phys. Rev. B* **75**, 155113 (2007).
- [34] K. Haule, Exact Double Counting in Combining the Dynamical Mean Field Theory and the Density Functional Theory, *Phys. Rev. Lett.* **115**, 196403 (2015).
- [35] J. Moulder and J. Chastain, *Handbook of X-ray Photoelectron Spectroscopy: A Reference Book of XPS Data* (Physical Electronics Division, Perkin-Elmer Corporation, 1992).
- [36] S. Sarkar, P. Sadhukhan, V. K. Singh, A. Gloskovskii, K. Deguchi, N. Fujita, and S. R. Barman, Bulk electronic structure of high-order quaternary approximants, *Phys. Rev. Res.* **3**, 013151 (2021).
- [37] L. Baumgarten, C. M. Schneider, H. Petersen, F. Schäfers, and J. Kirschner, Magnetic x-ray dichroism in core-level photoemission from ferromagnets, *Phys. Rev. Lett.* **65**, 492 (1990).
- [38] J. G. Menchero, One-electron theory of core-level photoemission from ferromagnets, *Phys. Rev. B* **57**, 993 (1998).
- [39] J. J. Yeh and I. Lindau, Atomic subshell photoionization cross sections and asymmetry parameters: $1 \leq Z \leq 103$, *Atomic Data and Nuclear Data Tables* **32**, 1 (1985).
- [40] M. Kim and B. I. Min, Nature of itinerant ferromagnetism of SrRuO_3 : A DFT+DMFT study, *Phys. Rev. B* **91**, 205116 (2015).
- [41] R. S. Singh, V. R. R. Medicherla, and K. Maiti, Role of long range ferromagnetic order in the electronic structure of $\text{Sr}_{1-x}\text{Ca}_x\text{RuO}_3$, *Applied Physics Letters* **91**, 132503 (2007).
- [42] S. Ghosh, S. Ershadrad, V. Borisov, and B. Sanyal, Unraveling effects of electron correlation in two-dimensional Fe_nGeTe_2 ($n = 3, 4, 5$) by dynamical mean field theory, *npj Computational Materials* **9**, 1 (2023).
- [43] T. J. Kim, S. Rye, and M. J. Han, Fe_3GeTe_2 : a site-differentiated Hund metal, *npj Computational Materials* **8**, 1 (2022).
- [44] A. Paul and T. Birol, Applications of DFT + DMFT in materials science, *Annu. Rev. Mater. Res.* **49**, 31 (2019).
- [45] G. Kotliar, S. Y. Savrasov, K. Haule, V. S. Oudovenko, O. Parcollet, and C. A. Marianetti, Electronic structure calculations with dynamical mean-field theory, *Rev. Mod. Phys.* **78**, 865 (2006).
- [46] Z. Zhou, S. K. Pandey, and J. Feng, Dynamical correlation enhanced orbital magnetization in VI_3 , *Phys. Rev. B* **103**, 035137 (2021).
- [47] Y. O. Kvashnin, A. N. Rudenko, P. Thunström, M. Rösner, and M. I. Katsnelson, Dynamical correlations in single-layer CrI_3 , *Phys. Rev. B* **105**, 205124 (2022).
- [48] K. Maiti, A. Kumar, D. D. Sarma, E. Weschke, and G. Kaindl, Surface and bulk electronic structure of $\text{La}_{1-x}\text{Ca}_x\text{VO}_3$, *Phys. Rev. B* **70**, 195112 (2004); K. Maiti, R. S. Singh, V. R. R. Medicherla, S. Rayaprol, and E. V. Sampathkumaran, Origin of charge density wave formation in insulators from a high resolution photoemission study of BaIrO_3 , *Phys. Rev. Lett.* **95**, 016404 (2005); S. Bansal, R. K. Maurya, A. Ali, B. H. Reddy, and R. S. Singh, Role of electron correlation and disorder on the electronic structure of layered nickelate $(\text{La}_{0.5}\text{Sr}_{0.5})_2\text{NiO}_4$, *Phys. Rev. Materials* **7**, 064007 (2023).
- [49] M. R. Norman, H. Ding, M. Randeria, J. C. Campuzano, T. Yokoya, T. Takeuchi, T. Takahashi, T. Mochiku, K. Kadowaki, P. Guptasarma, and D. G. Hinks, Destruction of the Fermi surface in underdoped high-Tc superconductors, *Nature* **392**, 157 (1998); R. S. Singh, V. R. R. Medicherla, K. Maiti, and E. V. Sampathkumaran, Evidence for strong $5d$ electron correlations in the pyrochlore $\text{Y}_2\text{Ir}_2\text{O}_7$ studied using high-resolution photoemission spectroscopy, *Phys. Rev. B* **77**, 201102 (2008); B. H. Reddy, A. Ali, and R. S. Singh, Role of disorder and strong $5d$ electron correlation in the electronic structure of $\text{Sr}_2\text{TiIrO}_6$, *Europhysics Letters* **127**, 47003 (2019).
- [50] H. Hegger, C. Petrovic, E. G. Moshopoulou, M. F. Hundley, J. L. Sarrao, Z. Fisk, and J. D. Thompson, Pressure-Induced Superconductivity in Quasi-2D CeRhIn_5 , *Phys. Rev. Lett.* **84**, 4986 (2000).
- [51] C. Krellner, T. Förster, H. Jeevan, C. Geibel, and J. Sichelschmidt, Relevance of Ferromagnetic Correlations for the Electron Spin Resonance in Kondo Lattice Systems, *Phys. Rev. Lett.* **100**, 066401 (2008).
- [52] Z. Fisk, D. W. Hess, C. J. Pethick, D. Pines, J. L. Smith, J. D. Thompson, and J. O. Willis, Heavy-Electron Metals: New Highly Correlated States of Matter, *Science* **239**, 33 (1988).
- [53] J. Mravlje, M. Aichhorn, T. Miyake, K. Haule, G. Kotliar, and A. Georges, Coherence-Incoherence Crossover and the Mass-Renormalization Puzzles in Sr_2RuO_4 , *Phys. Rev. Lett.* **106**, 096401 (2011).
- [54] Y. O. Kvashnin, O. Grånäs, I. Di Marco, M. I. Katsnelson, A. I. Lichtenstein, and O. Eriksson, Exchange parameters of strongly correlated materials: Extraction from spin-polarized density functional theory plus dynamical mean-field theory, *Phys. Rev. B* **91**, 125133 (2015).

[55] U. Mizutani, *Introduction to the Electron Theory of Metals*
(Cambridge University Press, 2001).

Supplemental Material for “Manifestation of incoherent-coherent crossover and non-Stoner magnetism in the electronic structure of Fe_3GeTe_2 ”

Deepali Sharma,¹ Asif Ali,¹ Neeraj Bhatt,¹ Rajeswari Roy Chowdhury,¹
Chandan Patra,¹ Ravi Prakash Singh,¹ and Ravi Shankar Singh^{1,*}

¹*Department of Physics, Indian Institute of Science Education and Research Bhopal,
Bhopal Bypass Road, Bhauri, Bhopal 462066, India*

(Dated: August 29, 2024)

NOTE 1: EXPERIMENTAL DETAILS AND ANALYSIS

X-ray photoemission survey scan :

The survey scan collected using Al K_α radiation at 30 K is shown in Fig. S1. The Fe 2p, Te 3d and Ge 3d core levels are marked with red colour which are also shown in the Fig. 1(b) of the main text. Absence of O 1s and C 1s features in the spectra as shown in the insets, along with bright spots in the LEED pattern exhibiting hexagonal symmetry, confirms high quality and clean sample surface.

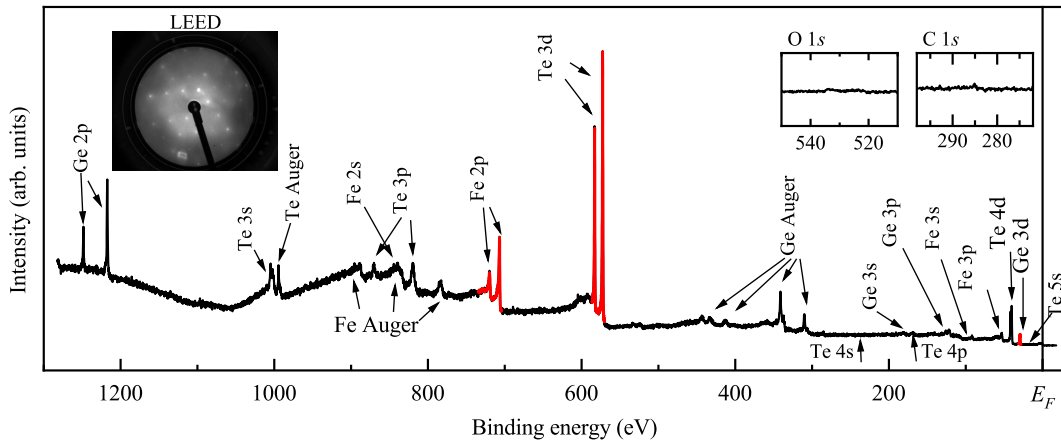


Fig. S1. Survey scan of Fe_3GeTe_2 collected using Al K_α radiation at 30 K. All the core level and Auger features are marked by arrows. The LEED pattern exhibiting hexagonal symmetry of the spots is shown in the inset on the left. Two insets on the right show the absence of O 1s and C 1s features in the corresponding binding energy regions.

* rssingh@iiserb.ac.in

Temperature dependent high-resolution spectral density of states (SDOS):

The photoemission intensity can be expressed as $I(E) = DOS(E, T) * \Gamma^e * \Gamma^h * G(E) * F(E, T)$, where Γ^e (Γ^h) represents lifetime broadening of photoelectron (photohole), F and G represent Fermi-Dirac (FD) distribution function and instrumental resolution broadening, respectively [1]. Since the photoelectrons and photoholes are long-lived close to the Fermi energy, E_F , the photoemission intensity divided by the resolution broadened FD function depicts the spectral DOS (SDOS) $[I(E)/(G(E) * F(E, T))]$. SDOS obtained using this method is shown in the main text (Fig. 3(b)). Since the FD distribution function (also resolution broadened) follows the relation $F(E)+F(-E) = 1$, thus symmetrization of the photoemission spectra around E_F $[I(E)+I(-E)]$ also provides a good description of SDOS, assuming DOS to be a smooth function around E_F . The SDOS obtained by this method (symmetrization) has been shown in Fig. S2, clearly indicating emergence of the quasiparticle peak (~ 40 meV) and the peculiar behavior of SDOS at E_F , same as the results shown in Fig. 3(b) and (c) of the main text.

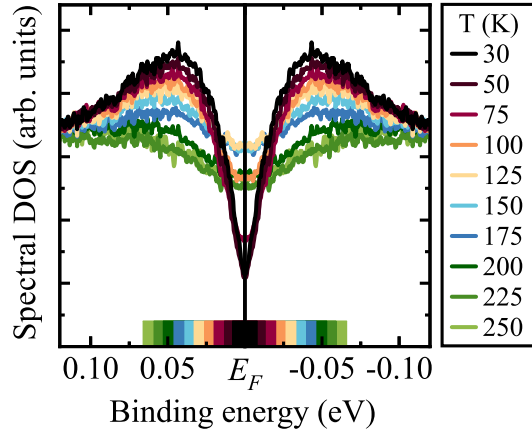


Fig. S2. Symmetrization of the high-resolution He I spectra in the vicinity of E_F for different temperature. Bottom color bar indicates the thermal energy ($\pm 3k_B T$) range.

NOTE 2: COMPUTATIONAL DETAILS AND ANALYSIS

Non-magnetic DFT and DFT + U results :

Figure S3 shows the total density of states (DOS) and partial DOSs of Fe I $3d$, Fe II $3d$, Ge $4p$ and Te $5p$ obtained from the non-magnetic (NM) DFT calculation. The partial DOSs show contributions from inequivalent Fe within ± 2 eV binding energy (BE) while the dominant contributions from Te $5p$ and Ge $4p$ states appear above 2 eV BE, in

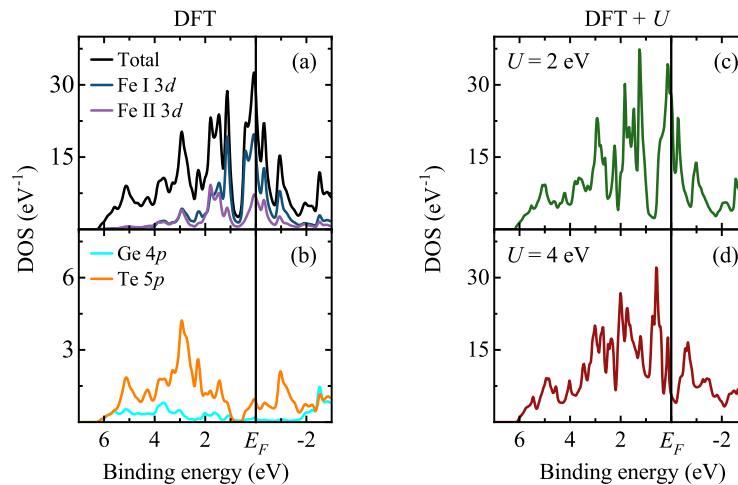


Fig. S3. (a) Total DOS and partial DOSs of Fe I $3d$ and Fe II $3d$, and (b) partial DOSs of Ge $4p$ and Te $5p$ obtained from NM DFT calculation. Total DOS obtained from NM DFT+ U calculations (c) for $U = 2$ eV, and (d) for $U = 4$ eV.

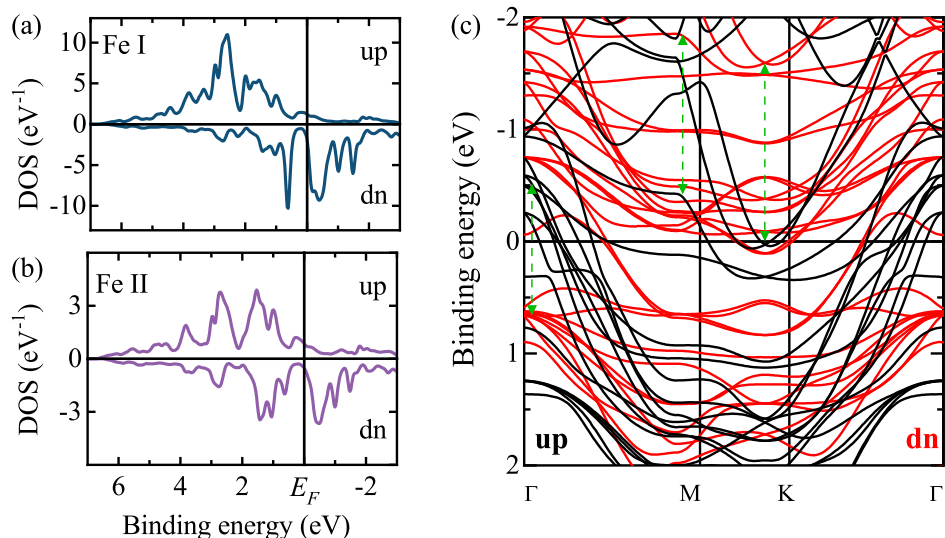


Fig. S4. Spin-polarized partial DOSs for (a) Fe I and (b) Fe II using FM DFT calculation. (c) Spin-polarized band dispersions along high symmetry directions using FM DFT calculation. The vertical green dashed lines are guide to the eyes for approximate exchange splitting of bands.

agreement with experimental valence band spectra. Total DOS obtained from DFT+ U calculations ($U = 2$ eV and 4 eV) are shown in the right panels of Fig. S3. The inclusion of U in DFT leads to shift of 1.5 eV feature towards higher BE and decrease in the DOS at E_F , in contrast to the experimental spectra where the Fe 3d band appears within the 1.5 eV BE.

Ferromagnetic DFT and DFT+ U results :

Results of the ferromagnetic (FM) DFT calculations are shown in the Fig. S4 where, spin-polarized 3d states corresponding to Fe I and Fe II are shown in panels (a) and (b), respectively. Large exchange splitting of spin-polarized DOS is clearly evident for both the inequivalent Fe alongwith dominant contributions of 3d states appearing beyond 2 eV BE. FM DFT calculation also overestimates spin magnetic moments ($2.46 \mu_B$ and $1.59 \mu_B$ for Fe I and Fe II, respectively), in comparison to the experimental result [2]. $\text{DOS}(E_F) = 3.31 \text{ states eV}^{-1} \text{ f.u.}^{-1}$ leads to Sommerfeld coefficient ($\gamma_{\text{DFT}} = \pi^2 k_B^2 \text{DOS}(E_F)/3$) of $7.79 \text{ mJ mol}^{-1} \text{ K}^{-2}$. With the experimentally obtained large γ value for Fe₃GeTe₂ [3], the FM DFT calculation suggests a significant quasiparticle mass enhancement $m^*/m_{\text{DFT}} = \gamma/\gamma_{\text{DFT}} = 14.12$. Spin-polarised band dispersion along high symmetry directions are shown in Fig. S4 (c) where, the dashed vertical lines show approximate exchange splittings of bands. The spin-polarised total DOS obtained within FM DFT and FM DFT+ U for $U = 2$ eV and $U = 4$ eV are shown in Fig. S5 (a)-(c). The inclusion of U in FM DFT calculations lead to further enhancement of exchange splitting and magnetic moment. For $U = 2$ eV and 4 eV, the obtained spin magnetic moments are $2.79 \mu_B$ ($1.76 \mu_B$) and $3.08 \mu_B$ ($2.38 \mu_B$) for Fe I (Fe II), respectively.

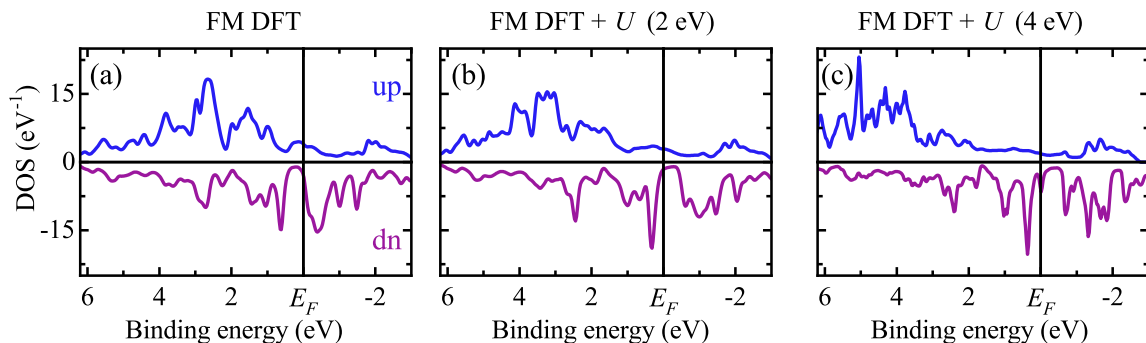


Fig. S5. Spin-polarized total DOS using (a) FM DFT, (b) FM DFT+ U (2 eV) and (c) FM DFT+ U (4 eV), calculations.

-
- [1] K. Maiti, A. Kumar, D. D. Sarma, E. Weschke, and G. Kaindl, *Phys. Rev. B* **70**, 195112 (2004); K. Maiti, R. S. Singh, V. R. R. Medicherla, S. Rayaprol, and E. V. Sampathkumaran, *Phys. Rev. Lett.* **95**, 016404 (2005); S. Bansal, R. K. Maurya, A. Ali, B. H. Reddy, and R. S. Singh, *Phys. Rev. Materials* **7**, 064007 (2023).
- [2] R. R. Chowdhury, S. DuttaGupta, C. Patra, O. A. Tretiakov, S. Sharma, S. Fukami, H. Ohno, and R. P. Singh, *Scientific Reports* **11**, 14121 (2021).
- [3] J.-X. Zhu, M. Janoschek, D. S. Chaves, J. C. Cezar, T. Durakiewicz, F. Ronning, Y. Sassa, M. Mansson, B. L. Scott, N. Wakeham, E. D. Bauer, and J. D. Thompson, *Phys. Rev. B* **93**, 144404 (2016).